A Paracrystalline Description of Defect Distributions in Wüstite, Fe$_{1-x}$O

T. R. Welberry and A. G. Christy

Research School of Chemistry, Australian National University, Canberra, ACT 0200, Australia

Diffuse X-ray scattering data from a crystal of wüstite, Fe$_{0.943}$O, are presented. Satellite reflections corresponding to an incommensurate repeat distance of ~2.7a in all three cubic directions were observed (the P' phase). The satellites were diffuse, anisotropically elongated, interconnected by weaker continuous streaks, and negligible in intensity beyond first order. Monte Carlo computer simulations have been carried out which demonstrate that this diffraction behavior is consistent with defect clusters forming a *paracrystalline* (or highly distorted) lattice. The paracrystalline distribution which best fits the observations is such that the spacing between defects tends to be maintained fairly constant, but relative lateral translations may occur more variably. When these lateral translations are suppressed, additional superlattice peaks appear which are consistent with the P″ phase diffraction patterns. The diffuse satellites are systematically more intense on the low-angle side of a Bragg reflection than on the high-angle side. This behavior may be understood in terms of the well-known *atomic size effect* and is consistent with a local contraction of the structure around regions of low scattering power (defect clusters) and compensating expansion in other parts of the structure. © 1995 Academic Press, Inc.

INTRODUCTION

Unlike the neighboring cations in the periodic table (Mn, Co, Ni), iron does not form a stable monoxide. The wüstite phase, Fe$_{1-x}$O, remains stable to the lowest temperature (576°C) for the eutectoid composition x = 0.055 (1). Below that temperature, wüstite bulk compositions are represented at thermodynamic equilibrium by a mixture of metallic iron and magnetite, Fe$_3$O$_4$. The composition range increases with pressure and temperature, the smallest x value obtained to date for a single-phase sample being 0.02 at 7 GPa and 1200°C (2). Quenched samples of wüstite can be studied under ambient conditions. However, heat treatment at temperatures as low as 225–300°C is sufficient to initiate decomposition into a multiphase mixture (3, 4). The only evidence for the existence of stoichiometric FeO is provided by Mössbauer spectra from such a thermally decomposed sample, which shows negligible Fe^{3+} in the oxide phase (5). This material

appears to be a transient intermediate between nonstoichiometric wüstite and iron.

Wüstite occurs frequently as an intermediate in iron redox reactions. It acts as a catalyst in carbon gasification (6), aromatic hydrocarbon cracking (7), and noxious gas conversion (8). In solid solution with MgO, it appears to be a major constituent of the Earth's lower mantle (9). Furthermore, the crystal structure of wüstite is a defective variant of that of rock salt. Chemically, the relationship between wüstite and stoichiometric FeO can be expressed as

$$3Fe^{2+} = 2Fe^{3+} + [\ ],$$
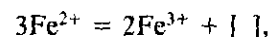
where [ ] represents a cation vacancy. However, Fe^{2+}, Fe^{3+}, and vacancies do not form a simple solid solution on the rock salt cation sublattice. Some tetrahedral interstices of the structure were found to be occupied by Fe in neutron and X-ray diffraction studies (10–13). Manenc *et al.* (14) reported the occurrence of an incommensurate superstructure with cubic a parameter about 2.6 times that of the ideal rock salt subcell. Koch and Cohen (12) reported this value more precisely as 2.73 for x = 0.077, decreasing to 2.61 for x = 0.098. The superlattice parameter also decreased to 2.61a for their smallest x value (0.053), but they noted that the superstructure diffraction peaks were extremely broad, so this value is not accurately determined. Other values collated by Bauer and Pianelli (15) cluster strongly around 2.68a. Yamamoto (16) reported 2.51a for the x = 0.098 composition. The small and unsystematic variation in the modulation vector with composition suggests that thermal history may be the most important factor in determining the size of the supercell.

Thermodynamic data for wüstite (17–19) indicate that x does not increase as the 1/6th power of $p(O_2)$ as would be expected for an ideal solid solution of vacancies and both iron species. The dependence is between 3rd power (small x) and 10th (high x), and x decreases with temperature at constant $p(O_2)$ rather than increasing as would be expected (20); there is evidently considerable defect

clustering in the structure. Various different cluster geometries have been proposed, but there is not yet general agreement on which are correct. The situation is further complicated by the occurrence of two ordered phases for oxidized compositions $x > 0.07$. These were detected in the high-temperature work of Vallet and Raccah (17, 18), who defined compositional and temperature limits of occurrence for them; they have also been characterized in quenched samples by electron microscopy (3, 4) . The phase relations and physical properties of the different wüstites, Fe, and Fe_3O_4, have been thoroughly reviewed (20, 21).

Using the terminology of Manenc (3), the hypothetical fully disordered phase is P, the $2.6a$ cubic phase is P′. The next phase, P″, was refined as $5a \times 5a \times 5a$ polar orthorhombic in symmetry by Andersson and Sletnes (4) but may be $2.5a \times 5a$ orthorhombic (Nagakura et al. (22); third principal axis not characterized), and the third phase, P‴, is similar but more ordered, giving sharper diffraction spots. The lattice parameter study by Hayakawa et al. (23) indicates that there is no volume change associated with formation of the more ordered phases. Room-pressure subcell lattice parameters agree well with the linear relation a (Å) $= 4.334 - 0.478x$ (2). However, the data reviewed by Bauer and Pianelli (15) show a dependence of cell parameter on temperature of crystallization. $1300°C$ samples gave smaller a values than $700°C$ samples by about 0.01 Å, corresponding to a change in x of 0.02. This was interpreted as showing an increase in tetrahedral site occupancy relative to vacancy number at high temperature, although the opposite trend was reported in the neutron powder diffraction study of Radler et al. (24).

The defect cluster geometry and distribution in the P′ phase is clearly important to the stability of wüstite over the greater part of its range in pressure–temperature–composition space. In this paper, we present diffuse X-ray scattering data and simulated diffuse scattering patterns which provide constraints on the distribution of defect clusters and local atomic displacements. In the P′ phase the incommensurate satellites are diffuse, lie on diffuse streaks, and are of negligible intensity beyond first order. High-resolution electron micrographs of the P′ structure show considerable variation in vector length and intervector angles in the defect array (25). We show that this behavior is consistent with a description of the P′ phase as a *paracrystalline* array of defects embedded in the rock salt substructure. This simple model semiquantitatively describes the observed X-ray scattering behavior without presuming the incipient development of large, ordered supercells. An important distinction between the paracrystal and a more conventional incommensurate model is that the modulation wave vector displays a significant variation in magnitude and direction for the paracrystal.

The sample studied in the present work has $x = 0.057$, very close to the eutectoid composition (26); data for this composition of maximum thermal stability should help to elucidate why wüstite occurs with nonzero x and a complex defect structure, but not as stoichiometric FeO.

Wüstite diffuse scattering has been studied previously for various compositions at high temperature (840 and $900°C$) (27, 28). In Hayakawa et al. (27) the pattern of diffuse maxima around the Bragg peaks appears to have been similar to that seen in our sample. However, in Garstein et al. (28), the samples were more P″-like in diffraction behavior. Though the studies of Hayakawa et al. (27), as well as studies of quenched material (12, 16, 29, this study), have consistently found a local contraction of the lattice around the clusters, Garstein et al. (28) found that some of the cations adjacent to the defect clusters moved away from the clusters.

Defect Geometry

Attempts have been made to refine the modulated structure as a commensurate superstructure (12, 16, 30). The refinements all supported the concept of the defects being clusters of V_4T tetrahedra, where V is a vacant octahedral cation site and T is a tetrahedral cation. Such clusters were found to be more stable than smaller vacancy–interstitial aggregates by 1–2 eV per vacancy in the lattice energy calculations of Catlow and Fender (31). The wüstite samples examined in the diffraction studies were relatively oxidized ($x = 0.08$–0.10), so the clusters were large (three to four tetrahedra). The high-temperature neutron diffraction work (13) showed that the clusters increase in size with x. For a composition similar to that of this study ($x = 0.053$), the number of tetrahedra per cluster was calculated to be 1.1–1.4 ± 0.3 at $800°C$. The types of cluster geometry that are possible proliferate rapidly with increasing number of component tetrahedra. X-ray and neutron diffraction (32, 33, 28) and lattice energy calculations (31, 34) have not yet fully characterized cluster geometry as a function of composition and temperature. In more oxidized wüstites, a range of defect clusters V_7T_2, $V_{10}T_3$, $V_{13}T_4$, etc. appears to be present (24). For Fe-rich compositions like that of this study ($x = 0.057$), the possibilities are more limited.

Assume that there is one defect cluster per "supercell." For the observed $k = 2.7a$ modulation, the defects are characterized by a mean $4k^3x = \Delta = (V-T) = 4.5$. This value is proportional to the cube of the modulation wave vector, so small uncertainties in k affect Δ disproportionately. For $k = 2.5a$, $\Delta = 3.56$ at this composition.

For a single V_4T tetrahedron, $\Delta = 3$. Pairs of tetrahedra may be linked through corner-sharing of a vacancy (V_7T_2; $\Delta = 5$) or edge-sharing (V_6T_2; $\Delta = 4$). Lattice energy calculations fail to demonstrate a consistent preference

for edge- or corner-sharing of the tetrahedral clusters (31, 34). However, the simplest tetrahedral groups with $\Delta >$ 4 are the corner-sharing pairs. Therefore, it seems likely that our defect clusters are a mixture of isolated tetrahedra (25%) and V_7T_2 groups (75%). The percentages are uncertain due to the k^3 dependence of Δ. For $k < 2.6a$ and $x = 0.057$, single tetrahedra would be expected to predominate.

For the simulation work of the present study, where the relative dispositions of neighboring clusters is more important than the exact identity of each cluster, all have been assumed to be single V_4T tetrahedra.

EXPERIMENTAL

The wüstite sample examined in the present study was taken from a single-crystal (001) slice approximately 1.5 mm thick and 6 mm in diameter. This was a section of a boule grown by the floating-zone technique (35). The boule had been equilibrated for 60 hr with a CO_2–CO gas mixture chosen to yield the $x = 0.055$ wüstite composition at equilibrium. Powder diffraction and density measurements confirmed the final composition as $x = 0.057$. Reflected light microscopy and Laue diffraction confirmed the nature of the sample and the absence of iron or magnetite precipitates (26).

A fragment approximately 1.5×2 mm was broken from the slice. This was mounted on a goniometer and orientated so as to rotate about a [001] direction. The crystal was then ground into a cylinder ($\sim$0.7 mm diameter) using the crystal grinder described by Wood et al. (36). Preliminary X-ray examination showed the presence of powder rings due to surface damage. Therefore, the crystal was cleaned for a few minutes in concentrated HCl. This treatment removed the streaking satisfactorily.

Layers of diffraction data normal to $\mathbf{c}^*$ were collected using $MoK\alpha$ radiation on the position-sensitive-detector diffraction system described by Osborn and Welberry (37). Examples of these observed diffraction patterns in the form of gray-scale images are shown in Figs. 1a, 1b, and 1d. Intense FeK fluorescence from the sample was suppressed using an aluminium sheet of ca. 0.3 mm thickness as a filter. $\lambda/2$ scattering, which was initially quite obtrusive, was eliminated by use of an excitation potential of $\sim$32 kV, insufficent to excite emission of X-rays of this wavelength. These less-than-ideal experimental conditions, together with the fact that $MoK\alpha$ radiation is less-efficiently detected and gives relatively poor spatial resolution, provided data that were less satisfactory than we would normally expect to obtain. In order to obtain better signal-to-noise and improved spatial resolution, some later experiments were carried out using $CoK\alpha$ radiation, for which there are no fluorescence problems, but for which the accessible region of reciprocal space is
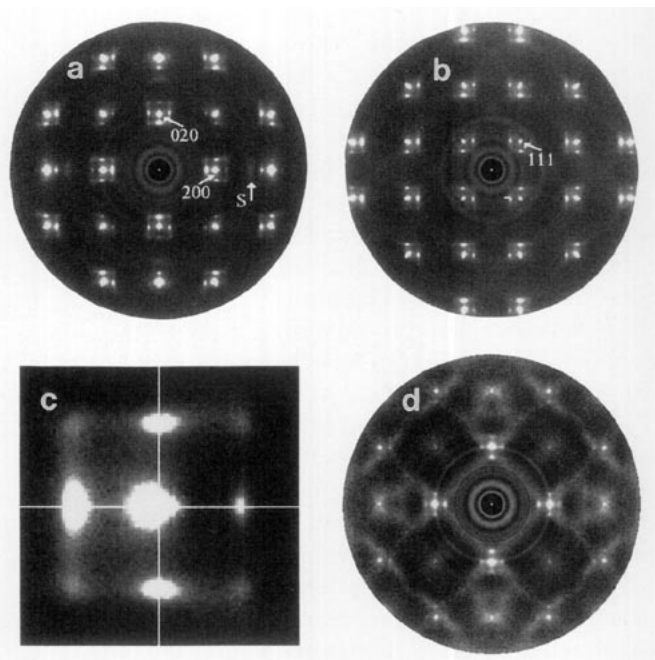

FIG. 1. Observed diffraction patterns. (a) The $(h\ k\ 0)$ section. (b) The $(h\ k\ 1)$ section. (c) An enlarged region of the $(h\ k\ 0)$ section around $(2\ 0\ 0)$. (d) The $(h\ k\ 0.4)$ section. (a), (b), and (d) were recorded using $MoK\alpha$. The maximum diffraction angle shown corresponds to $\sim$51° of 2θ. (c) was recorded using $CoK\alpha$ to obtain better resolution. The circular features seen in the $MoK\alpha$ pictures are due to parasitic scattering from the beam-stop. "S" indicates a second-order incommensurate peak.

restricted. Figure 1c shows a more detailed view of the region around the $(2\ 0\ 0)$ reciprocal point obtained using $CoK\alpha$. Figure 1d is included to show that there are more extended regions of diffuse scatter in addition to the incommensurate peaks. It is not the intention in the present paper to try to model this extended scattering but to concentrate on the incommensurate diffuse peaks.

PARACRYSTAL MODEL FOR DEFECT DISTRIBUTION

It is clear from Fig. 1 that not only are the incommensurate peaks themselves quite diffuse with very anisotropic shapes but there is also diffuse streaking connecting the peaks. This streaking is strongest in directions tangential to the vector from the nearest parent reflection. The peaks themselves are somewhat elongated in this same tangential direction. The other remarkable feature of the patterns is that there is very little evidence of higher-order satellite peaks. If we assume the basic modulation vectors are $\delta\mathbf{a_1}^*$, $\delta\mathbf{a_2}^*$, and $\delta\mathbf{a_3}^*$ then we observe peaks at $(h \pm n_1\delta, k \pm n_2\delta, l \pm n_3\delta)$ for $n_1, n_2, n_3 = 0$ or 1 only. The only exception to this is a very broad second-order peak at $(4\text{-}2\delta, 0, 0)$, indicated by "S" in Fig. 1a.

These features taken together are characteristic of the diffraction patterns of highly distorted lattices, for which Hosemann and Bagchi (38) coined the name *paracrystals*,

and for which some of the concepts were further developed by us under the name of Gaussian growth–disorder models (39–41). In this section we show how the diffraction pattern of wüstite can be understood in terms of a model in which defects are situated on the sites of such a highly distorted (or *paracrystalline*) lattice. Direct evidence for this as a viable model is afforded by a brief report by Iijima (25) in which an electron micrograph of a direct image of a defect distribution was shown, very reminiscent of paracrystalline distributions.

If the real-space distribution can be considered to be a perfect lattice of ideal wüstite *multiplied* by a second larger-scale paracrystal distribution function describing the position of the defects, the diffraction pattern will then consist of the ideal wüstite diffraction pattern *convoluted* with the diffraction pattern of the paracrystal distribution. That is, around each parent Bragg peak appears the *motif* of scattering which is the Fourier transform of the paracrystal distribution. However, it is clear from the observed data that the distribution around each parent Bragg peak is asymmetric, those peaks occurring at $-\delta$ being invariably much stronger than those at $+\delta$. Such asymmetry is again a very characteristic diffraction effect caused by local strains induced by differences in atomic size, the so-called atomic size effect (see (42–44)). In the present case it is necessary to assume that the ideal wüstite structure relaxes around the defect sites, in such a way that the average lattice spacing is decreased in the neighborhood of the defects (which scatter less strongly than the rest of the structure) and is relatively increased elsewhere. To test these suppositions we constructed a computer model from which diffraction patterns were calculated for comparison with the observed patterns.

COMPUTER MODELING

With the advances in computer power in recent years it has become feasible to model disordered structures in three dimensions. In these studies a model crystal of typical dimensions 32 × 32 × 32 unit cells is set up and, using interatomic interactions of various kinds, allowed to develop via Monte Carlo or other types of computer simulation to obtain a final set of atomic positions, site occupancies, etc. from which a model diffraction pattern can be calculated. Such methods have been successfully applied to a quite diverse range of problems (45–48). At present this size model represents something close to a practical upper limit, since simulation time and subsequent calculation of the diffraction pattern become prohibitively long if substantially larger samples are used. In the present case this imposes a severe restriction on the effectiveness with which a paracrystalline lattice of defects can be introduced into the wüstite lattice, since the

mean spacing of such a lattice, $\sim 2.7 \times$ the cell repeat, means that only about 12–13 defects can be inserted in any direction in the lattice and the variation in spacing and orientation of the basic paracrystal vectors, which are characteristic of a given paracrystalline lattice, can only be rather poorly represented in such a small sample. For this reason, in what follows, we initially concentrate on 2D models, where the various effects can be more adequately demonstrated. The observed zero-level ($h\ k\ 0$) diffraction pattern (Fig. 1a) corresponds to a projection of the structure down the crystallographic c-axis, and we attempt to model this. Using comparable computer resources, simulation in 2D can be carried out on samples corresponding to 256×256 unit cells and the number of defects in a given direction, (~ 100) is sufficient to allow adequate representation of the variation in the paracrystalline lattice.

Finally, in order to demonstrate that the same effects do also hold in 3D we present some results for 3D simulations, for which, however, the paracrystal distributions cannot be so adequately represented.

GENERATION OF THE PARACRYSTAL ARRAYS

The paracrystalline lattices used in the present work were generated using the Gaussian growth-disorder algorithms (39, 40) examples of which were also discussed in Welberry (41).

$X_{i,j}$ is a normally distributed (Gaussian) random variable with zero mean and unit variance, associated with the i,jth site of a 2D lattice. The probability that $X_{i,j}$ takes a particular value given the values of the variables on the adjacent sites $X_{i-1,j}$, $X_{i,j-1}$, $X_{i-1,j-1}$ is given by the expression

$$P(X_{i,j}/X_{i-1,j}, X_{i,j-1}, X_{i-1,j-1}) = K \exp \tag{1}$$
$$-\left\{\frac{(X_{i,j} - rX_{i-1,j} - sX_{i,j-1} + rsX_{i-1,j-1})^2}{2(1 - r^2)(1 - s^2)}\right\}.$$

The right-hand side of this equation is a Gaussian with a mean of $rX_{i-1,j} + sX_{i,j-1} - rsX_{i-1,j-1}$ and variance of $(1 - r^2)(1 - s^2)$. The whole array of $X_{i,j}$ values may thus be generated using [1] in conjunction with a pseudorandom number generator which produces Gaussian distributed random numbers. Similar (but simpler) formulae for the two 1D boundaries also exist, and these must be set up first. Then use of [1] leads to a distribution that is immediately stationary and has nearest-neighbor correlations given by the parameters r and s. In particular,

$$\langle X_{i,j}X_{i-1,j} \rangle = r; \ \langle X_{i,j}X_{i,j-1} \rangle = s; \ \langle X_{i,j}X_{i-1,j-1} \rangle = rs. \tag{2}$$

If $X_{i,j}$ is taken to represent an atomic displacement in the x-direction then r represents a longitudinal correlation (with the displacement and correlation in the same direction) and s a transverse correlation (displacement and correlation at right angles). To create a 2D paracrystal involving both x- and y-displacements, a second set of random variables, $Y_{i,j}$, with identical transverse and longitudinal correlations is required. The two independent sets of Gaussian variables $X_{i,j}$ and $Y_{i,j}$ may be then be used to construct the distribution of defects in the wüstite lattice, as follows.

In projection the face-centered cubic array of Fe atoms in wüstite appears as a simple square array (see Fig. 2). For the present study we neglect entirely the oxygen atoms. This is justified on two grounds. Since they form a complete array the O atoms will contibute to the diffuse scattering only as a result of displacements from their average sites, and second, they have much smaller scattering factors than Fe and thus only contribute $\sim 10\%$ of the total scattered intensity. We use as a single defect a cluster consisting of a tetrahedron of Fe vacancies together with an interstitial Fe^{3+} ion. In projection this appears as a square of four vacant Fe sites with the Fe^{3+} ion at the center.

We label the Fe sites, which in 2D occur on a simple 2.15 Å square lattice, by indices n and m, where $1 < n$, $m < 512$. Defects, made by removal of Fe from the sites $n, m; n + 1, m; n, m + 1; n + 1, m + 1$ and replacement with an Fe^{3+} at $n + \frac{1}{2}, m + \frac{1}{2}$, are inserted for n,m given by

$$n = \text{nint}(5.4i + \sigma X_{i,j})$$
$$m = \text{nint}(5.4j + \sigma Y_{i,j}),\qquad [3]$$

where *nint* means "nearest integer," and σ is a standard deviation used to modify the originally unit variance of the random variables. The indices i and j vary over the paracrystalline array. In Fig. 3 we show two examples to
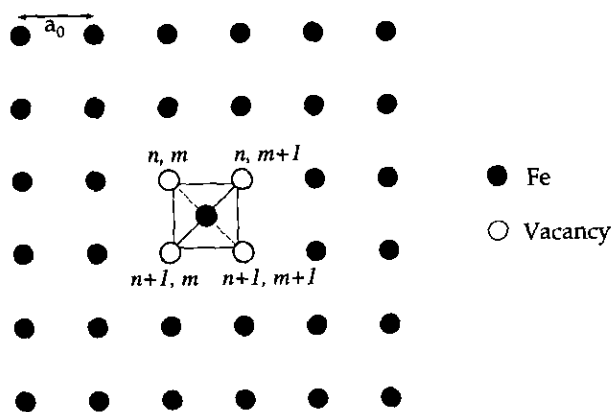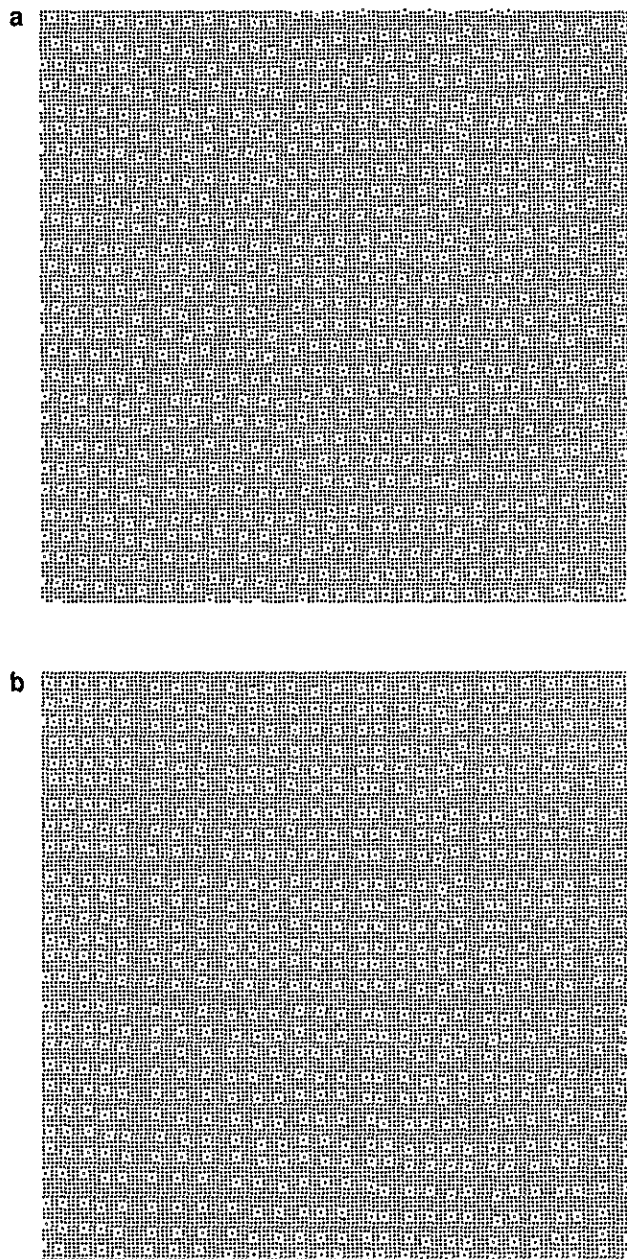
FIG. 3. Plots of regions of the 2D paracrystal defect distributions corresponding to the examples whose diffraction patterns are shown in Figs. 4a and 4b. In (a) the longitudinal correlation, $r = 0.99$ and the transverse correlation, $s = 0.95$. In (b) the longitudinal correlation, $r = 0.95$ and the transverse correlation, $s = 0.99$. In both cases the variation of the position of the defects about an underlying regular lattice, $\sigma = 2.5 \times a_0$, where $a_0 = a/2$ is the repeat distance in the projected wüstite lattice.

FIG. 2. Schematic diagram showing the form of a tetrahedral defect cluster in the 2D simulations and the labeling of the sites.

demonstrate the effect of r and s on the resulting distribution of defects. In both of these examples σ was 2.5 indicating that a given cluster may vary from a position on a perfectly regular array with a standard deviation corresponding to $2.5 \times a_0$, where $a_0 = a/2$ is the repeat distance in the projected wüstite lattice. This variation corresponds

to ~46% of the paracrystal lattice repeat. In Fig. 3a the longitudinal correlation r is dominant, while in Fig. 3b the transverse correlation s is dominant. In Fig. 3a the spacing between defects is maintained fairly rigidly while the relative lateral displacement is more variable. In Fig. 3b the spacing between defects is more variable but their relative lateral displacements are small, resulting in rather straighter rows of defects. The diffraction patterns calculated from these two distributions, using the algorithm of Butler and Welberry (49), are shown in Figs. 4a and 4b, respectively. For these calculations all atoms were assumed to be situated exactly on the idealized sites depicted. It is clear from these two examples that, although these patterns exhibit no asymmetry, the orientation of the streaks in Fig. 4a is similar to that in the X-ray patterns, while that in Fig. 4b is not. Similarly, the satellite peaks in Fig. 4a are elongated in the same direction as in the X-ray pattern, whereas in Fig. 4b they are not.

RELAXATION AROUND THE CLUSTERS

A simple Monte Carlo algorithm was devised to introduce size-effect distortions around the defects, which had been incorporated into the 2D lattice as described above. For the present work we assume a simple interaction potential in which harmonic (Hooke's law) springs connect neighboring primary lattice sites in the $\langle 10 \rangle$ and $\langle 11 \rangle$ directions. The Hamiltonian E is given by

$$E = \sum_{a,b} C_{ab}(R_{ab} - d_{ab})^2. \qquad [4]$$

Here the summation is over all nearest-neighbor pairs of sites in the $\langle 10 \rangle$ and $\langle 11 \rangle$ directions. The equilibrium length of the spring, R_{ab}, between a pair of sites ab was assumed to be equal to $(1 + \varepsilon_{ab})a_0$ for $\langle 10 \rangle$ springs and $\sqrt{2}(1 + \varepsilon_{ab})a_0$ for $\langle 11 \rangle$ springs. d_{ab} is the instantaneous length of a given intersite vector. After some initial experimentation to find appropriate values, the distortion parameter ε_{ab} was set to be -0.09 for vectors between a vacant site and an occupied site, $+0.012$ between two occupied sites, and 0.0 between two vacancies. After distortion this choice of parameters resulted in the mean cation/vacancy vector being reduced by ~3%. The strengths of the force constants, C_{ab}, for $\langle 10 \rangle$ and $\langle 11 \rangle$ springs were assumed equal since they are both projections of equivalent 3D vectors. The value of C_{ab} for springs between two vacant sites was taken to be 100 times greater than for any other spring so that the geometry of the basic vacancy cluster was rigidly maintained. The interstitial cation was placed at the center of mass of the rigid group of four vacancies.

Monte Carlo simulation was carried out for 50 cycles of iteration, a cycle defined as that number of individual steps necessary to visit each lattice site once on average.
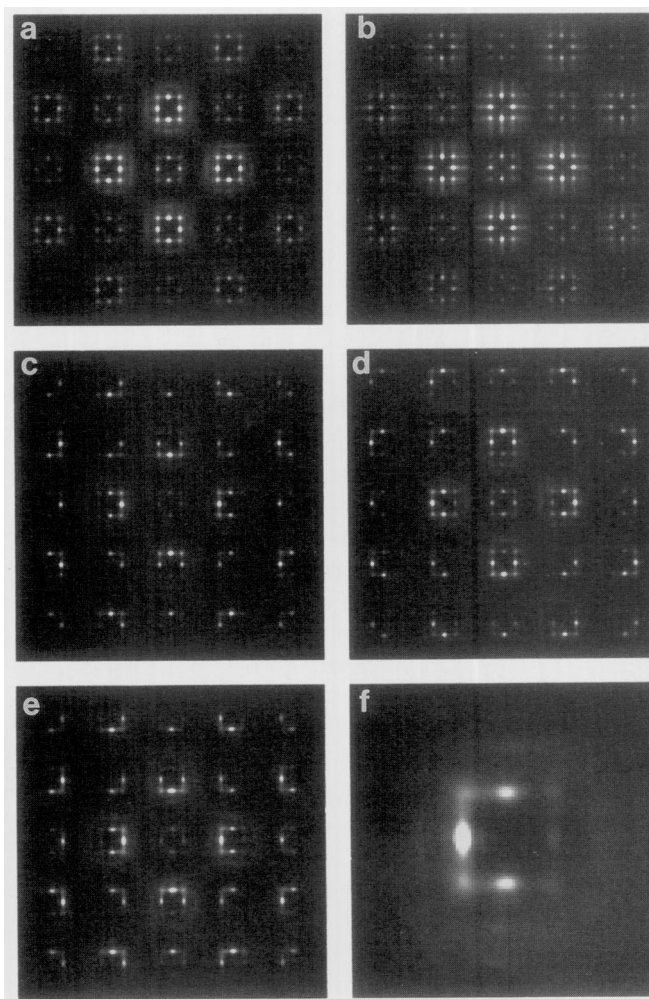

FIG. 4. Diffraction patterns calculated from the 2D simulations. (a) and (b) were calculated from the distributions shown in Figs. 3a and 3b, respectively, before the Fe atoms were allowed to relax from their ideal sites (see text for more details). (c) was calculated from the same distribution as (a) after relaxation in which surrounding atoms moved in toward a defect. (d) was calculated from the same distribution as (a) after relaxation in which surrounding atoms moved away from a defect. (e) was calculated from a similar model to (c) but in which the value of the transverse correlation, s, was reduced. (f) shows an enlarged region of (e) in the neighborhood of the (2 0 0) reciprocal point. In all the calculations the Bragg peaks were omitted.

After each cycle, lattice averages of the different types of nearest-neighbor distances were computed to monitor the progress of the relaxation. Final atomic positions were used to calculate the diffuse diffraction pattern, using the algorithm of Butler and Welberry (49). The diffraction pattern shown in Fig. 4c corresponds to the same example as Fig. 4a but after relaxation has been carried out. It is now clear that the asymmetry observed in the X-ray patterns is effectively reproduced, while the paracrystal-induced streaking between the diffuse peaks is maintained. To contrast this we show in Fig. 4d the same

example but in which the distortion has been applied in the opposite sense (i.e., the surrounding cation sites tend to move away from a defect). Here it is seen that the direction of the asymmetry is reversed.

While the asymmetry of the intensities in the peaks around a given parent Bragg peak is governed by the magnitude and direction of the distortion parameter, ε_{ab}, the relative magnitudes of the {10} and {11} peaks are affected by the values of the correlation parameters r and s. In the X-ray pattern of Fig. 1c it is seen that around the (2 0 0) Bragg peak the {10} satellites are much stronger and more distinct than the {11} satellites. In the calculated pattern of Fig. 4c, which otherwise corresponds well to the observed pattern, the {11} satellites are still relatively strong and quite distinct. In Fig. 4e a similar example is shown, in which the transverse correlation has been reduced from 0.95 to 0.9. Here the {11} satellites are now clearly diminished in intensity and sharpness. Figure 4f shows an enlargement of the region around the (2 0 0) position (cf. Fig. 1c). It should be noted in all of these calculated patterns that the Bragg peaks themselves are omitted.

SIMULATIONS IN 3D

The 2D results described above indicate that the form of the diffraction patterns can be explained in terms of a paracrystal-like distribution of defect clusters within a matrix of the ideal wüstite structure, followed by relaxation of the surrounding cations toward the defect cluster. For the reasons stated earlier we are unable to simulate in three dimensions paracrystalline arrays of defects in which the interdefect vector varies in length and orientation to an extent comparable to those 2D models. Nevertheless we made some calculations in 3D, with a reduced degree of variation, in order to show that the same basic distortion mechanism can be carried over to 3D and that this mechanism does account for the asymmetry of the satellite intensities in other nonzero layers of reciprocal space.

A property of the paracrystal distributions like those used in 2D is that the Gaussian-distributed displacements have a very large variance but at the same time have very high correlations to near-neighbor displacements. This high correlation means that despite the high variance of the actual position of the defects the interdefect distance has a fairly low variance. In fact it was shown (39) that the variance of the distance, σ_d, is related to the variance of the displacements, σ, and the correlation, r, between them, by

$$\sigma_d^2 = \sigma^2(1 - r).$$ [5]

It was also shown that rather similar diffraction patterns could be obtained for different values of σ if the correlation, r, was adjusted to maintain the same value of σ_d. While a value of $\sigma = 2.5 \times a_0$, where $a_0 = a/2$, was used for the 2D simulations described above, a value of no more than $\sigma = 1.0 \times a_0$ was found to be practical for the 3D simulations. With this 6.25-fold decrease in σ^2, the values of the correlations needed to produce similar diffraction patterns were correspondingly reduced. For the longitudinal correlation, $r = 0.99$, used in the 2D example of Fig. 4e. a value $r = 0.9375$ is now required to obtain the same value of σ_d. However, for the transverse correlation, $s = 0.9$, much smaller values of $s,t = 0.375$ are now required.

Apart from the limitation of needing to keep σ small imposed by the small sample size, simulation in 3D was otherwise very similar to the 2D description above. The basic distribution of defects was generated using a 3D Gaussian growth disorder algorithm, as described in Welberry and Carroll (40). Note that this defect array is a primitive cubic array. To create a 3D paracrystal involving x, y, and z displacements three independent sets of random variables, $X_{i,j,k}$, $Y_{i,j,k}$, and $Z_{i,j,k}$ with identical transverse and longitudinal correlations are required. These are then used to construct the distribution of defects in the wüstite lattice in a similar manner to that described for 2D.

The Fe sites occur on an fcc lattice of dimension $a = 4.30$ Å, with Fe atoms within the unit cell at (0,0,0), $(\frac{1}{2},\frac{1}{2},0)$, $(0,\frac{1}{2},\frac{1}{2})$, $(\frac{1}{2},0,\frac{1}{2})$. A tetrahedral defect can thus occur centered on any one of eight sites within the unit cell $(\frac{1}{4} + \frac{1}{2}n, \frac{1}{4} + \frac{1}{2}m, \frac{1}{4} + \frac{1}{2}l)$, where n, m, $l = 0$ or 1. It is convenient therefore to represent the position of a defect at any position in the lattice by the indices n, m, and l which take integral values on a primitive cubic lattice of spacing $a_0 = a/2$. For the arrays used in the present work $1 \leq n, m, l \leq 64$. Defects can occur in one of two different orientations. For $n + m + l$ even, tetrahedra point up along [111], while for $n + m + l$ odd, they point down.

Defects were placed at points in the wüstite lattice defined by n, m, l, where

$$n = \text{nint}(5.4i + \sigma X_{i,j,k})$$

$$m = \text{nint}(5.4j + \sigma Y_{i,j,k})$$ [6]

$$l = \text{nint}(5.4k + \sigma Z_{i,j,k}).$$

Here nint means nearest integer, and σ is a standard deviation used to modify the original unit variance of the random variables (in this case $\sigma = 1.0 \times a_0$). The indices i, j, k vary over the paracrystalline array. The value 5.4 is chosen to obtain a mean defect spacing of $2.7a$.

Relaxation around the defects was also carried out in an entirely analogous way to that described for two dimensions. With reference to Eq. [4], harmonic springs connected all $\langle 110 \rangle$ pairs of Fe sites and these springs had equilibrium lengths equal to $\sqrt{2}(1 + \varepsilon_{ab})a_0$ as before. The values of ε_{ab} that were used in the simulations were ~0.05 for an occupied and a vacant site, +0.008 for two occupied sites, and 0.0 for two vacant sites. These values for ε_{ab} result in atomic displacements in the neighborhood of defects of a comparable magnitude to those observed, for example, in the structure determination of Koch and Cohen (12).

In Figs. 5a and 5b we show two sections, $(h\ k\ 0)$ and $(h\ k\ 1)$, of the 3D diffraction pattern calculated from a simulation in which $\sigma = 1.0 \times a_0$, $r = 0.9375$, and $s,t = 0.375$. Note the similarity of Fig. 5a to the 2D pattern of Fig. 4c, although the peak shapes are not so anisotropic. Note also the general pattern of satellite spot intensities is in broad agreement with the observed patterns, for both the zero and first reciprocal layers.

For comparison we also carried out a simulation using the same values σ and r but with increased values of the transverse correlations, $s,t = 0.9$. Corresponding patterns for this simulation are shown in Figs. 5c and 5d. It is interesting to note that the patterns have now developed additional maxima between the original satellite peaks. These patterns are clearly reminiscent of the electron
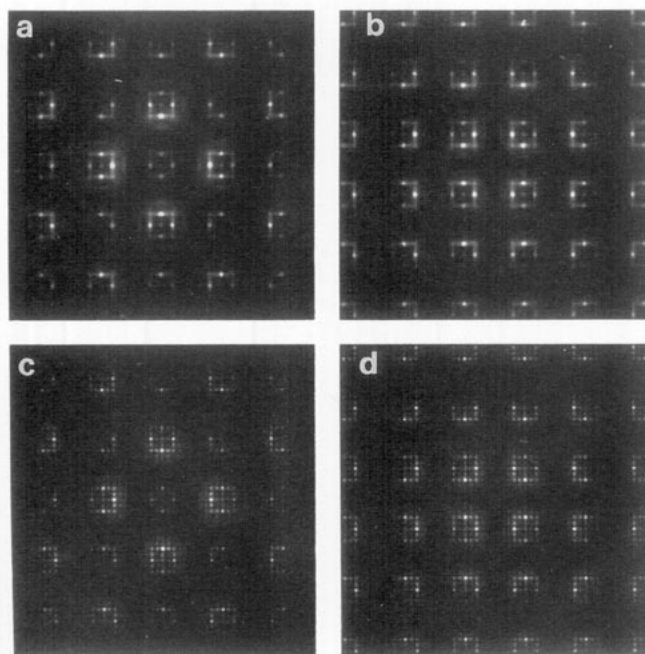

FIG. 5. Diffraction patterns calculated from the 3D simulations. (a) and (b) were calculated from a simulation in which the longitudinal correlation $r = 0.9375$ and the transverse correlations $s,t = 0.375$. For (c) and (d) $r = 0.9375$ and $s,t = 0.9$. (a) and (c) are of the $(h\ k\ 0)$ section. (b) and (d) are of the $(h\ k\ 1)$ section. For both examples $\sigma = 1.0 \times a_0$, where $a_0 = a/2$.

diffraction patterns of the P″ phase reported by Andersson and Sletnes (4).

CONCLUSION

In this paper we have shown how the diffraction patterns of a P′ phase crystal of wüstite can be understood in terms of a paracrystal-like distribution of defect clusters embedded in the normal rock salt substructure, together with a scheme for allowing the rock salt lattice to relax around the defects. For simplicity the defect clusters that have been assumed consisted of a tetrahedron of Fe vacancies together with an Fe^{3+} interstitial, the so-called V_4T cluster. Although it is appreciated that for the sample studied, for which the composition was $Fe_{1-x}O$ with $x = 0.057$, there will be appreciable numbers of larger clusters (such as corner-shared V_7T_2 or edge-shared V_6T_2 pairs of tetrahedra) it is expected that this will alter this description only in detail. The major features of the pattern are explained simply on the basis of the fact that the defect clusters represent regions of lower scattering power than the average lattice and the surrounding lattice relaxes in such a way that atoms *move in toward* the defects. With these broad features of the pattern accounted for in this way, it is our intention to explore the effects on the fine details of the diffraction pattern as different kinds of defect are introduced into the model. Work along these lines is now in progress.

The paracrystalline distribution that has been observed is such that there is a strong longitudinal correlation and a lesser transverse correlation. This means that the spacing between defects tends to be maintained fairly rigidly, but neighboring defects may more readily be translated laterally. The values estimated for these correlations are descriptive of the anisotropic shape of the satellites and cannot be compared with any previously reported data, although it is clear that the general appearance of the defect distributions that are generated show similarity to the high-resolution electron micrograph images of Iijima (25). When the transverse correlation is increased, the primitive paracrystal lattice is forced to "lock-in" to the underlying fcc lattice of the rock salt sublattice and form additional superlattice peaks consistent with the P″ phase diffraction patterns.

In addition to the incommensurate diffuse peaks we have observed weaker more extended diffuse streaking particularly on the incommensurate reciprocal layers (see Fig 1). In the present work we have made no attempt to explain these, but it seems likely that a detailed study of them could be rewarding in terms of trying to establish the defect cluster size distribution (over which there is still considerable debate in the literature) and a more detailed picture of the way in which the rock salt sublattice relaxes around them.

REFERENCES

1. L. S. Darken and R. W. Gurry, *J. Am. Chem. Soc.* **47**, 2876 (1945).
2. C. A. McCammon and L. Liu, *Phys. Chem. Miner.* **10**, 106 (1984).
3. J. Manenc, *Bull. Soc. Fr. Miner. Cristallogr.* **91**, 594 (1968).
4. B. Andersson and J. O. Sletnes, *Acta Crystallogr. Sect. A* **33**, 268 (1977).
5. B. Hentschel, *Z. Naturforsch. A* **25**, 1996 (1970).
6. Y. Ohtsuka, Y. Kuroda, Y. Tamai, and A. Tomita, *Fuel* **65**, 1476 (1986).
7. G. A. Simons, D. O. Ham, and G. Moniz (1986) *Morgantown Energy Technol. Cent. Report* DOE/METC-86/6042, and *in* "Proceedings, 6th Annu. Contr. Meet. Contam. Control. Coal-Deriv. Gas Streams."
8. Y. Tamaura, Eur. Patent Appl. EP 431,819 (Cl. B01D53/86). J.P. Appl. 89/308,568, 1991.
9. H-K. Mao, *Year Book Carnegie Inst. Washington* **73**, 511 (1974).
10. W. L. Roth, *Acta Crystallogr.* **13**, 140 (1960).
11. J. Smuts, *J. Iron Steel Inst. London* **204**, 237 (1966).
12. F. Koch and J. B. Cohen, *Acta Crystallogr. Sect. B* **25**, 275 (1969).
13. A. K. Cheetham, B. E. F. Fender, and R. I. Taylor, *J. Phys. C Solid State Phys.* **8**, L34 (1971).
14. J. Manenc, J. Bourgeot, and J. Benard, *C.R. Acad. Sci. Paris* **258**, 4528 (1964).
15. E. Bauer and A. Pianelli, *Mater. Res. Bull.* **15**, 177 (1980).
16. A. Yamamoto, *Acta Crystallogr. Sect. B* **38**, 1451 (1982).
17. P. Vallet and P. Raccah, *C.R. Acad. Sci.* **258**, 3679 (1964).
18. P. Vallet and P. Raccah, *Mem. Sci. Rev. Metall.* **62**, 1 (1965).
19. B. E. F. Fender and F. D. Riley, *J. Phys. Chem. Solids* **30**, 793 (1969).
20. S. Mrowec and A. Podgórecka, *J. Mater. Sci.* **22**, 4181 (1987).
21. R. M. Hazen and R. Jeanloz, *Rev. Geophys. Space Phys.* **22**, 37 (1984).
22. S. Nagakura, T. Ishiguro, and Y. Nakamura, (1983) *Lawrence Berkeley Laboratory Report* LBL-16031, Proceedings, 7th International Conference on High Voltage Electron Microscopy, p. 59.
23. M. Hayakawa, J. B. Cohen, and T. B. Reed, *J. Am. Ceram. Soc.* **55**, 160 (1972).
24. M. J. Radler, J. B. Cohen, and J. Faber, Jr., *J. Phys. Chem. Solids* **51**, 217 (1990).
25. S. Iijima, "Diffraction Studies of Real Atoms and Real Crystals," pp. 217. Australian Academy of Science, Canberra, 1974.
26. I. Jackson, S. K. Khanna, A. Revcolevschi, and J. Berthon, *J. Geophys. Res.* **95**, 21,671 (1990).
27. M. Hayakawa, M. Morinaga and J. B. Cohen, "Defects and Transport in Oxides" (M. S. Seltzer and R. I. Jaffee, Eds.), p. 177. Plenum, New York, 1974.
28. E. Garstein, T. O. Mason, and J. B. Cohen, *J. Phys. Chem. Solids* **47**, 759 (1986).
29. D. Neuschutz and N. Towhidi, *Arch. Eisenhuettenwes.* **41**, 303 (1970).
30. T. K. Hoang, A. D. Romanov, Ya. L. Shayovitch, and R. A. Zvinchuk, *Vestn. Leningr. Univ. Fiz. Khim.* **4**, 144 (1973).
31. C. R. A. Catlow and B. E. F. Fender, *J. Phys. C Solid State Phys.* **8**, 3267 (1975).
32. J. R. Gavarri, C. Carel, and D. Weiger, *J. Solid State Chem.* **29**, 81 (1979).
33. P. D. Battle and A. K. Cheetham, *J. Phys. C* **12**, 337 (1979).
34. C. R. A. Catlow, *Metal. Odlewnictwo* **13**, 31 (1987).
35. J. Berthon, A. Revcolevschi, H. Morikawa, and B. Touzelin, *J. Cryst. Growth* **47**, 736 (1979).
36. R. A. Wood, G. E. Tode, and T. R. Welberry, *J. Appl. Crystallogr.* **18**, 371 (1985).
37. J. C. Osborn and T. R. Welberry, *J. Appl. Crystallogr.* **23**, 476 (1990).
38. R. Hosemann and S. N. Bagchi, "Direct Analysis of Diffraction by Matter." North-Holland, Amsterdam, 1962.
39. T. R. Welberry, G. H. Miller, and C. E. Carroll, *Acta Crystallogr. Sect. A* **36**, 921 (1980).
40. T. R. Welberry and C. E. Carroll, *Acta Crystallogr. Sect. A* **38**, 761 (1982).
41. T. R. Welberry, *Rep. Prog. Phys.* **48**, 1543 (1985).
42. B. E. Warren, B. L. Averbach, and B. W. Roberts, *J. Appl. Phys.* **22**, 1493 (1951).
43. T. R. Welberry, *J. Appl. Crystallogr.* **19**, 382 (1986).
44. T. R. Welberry and B. D. Butler, *J. Appl. Crystallogr.* **27**, 205 (1994).
45. T. R. Welberry and T. N. Zemb, *J. Colloid Interface Sci.* **123**, 413 (1988).
46. T. R. Welberry and R. L. Withers, *Phys. Chem. Miner.* **17**, 117 (1990).
47. T. R. Welberry, *J. Appl. Crystallogr.* **24**, 203 (1991).
48. T. R. Welberry, B. D. Butler, J. G. Thompson, and R. L. Withers, *J. Solid State Chem.* **106**, 461 (1993).
49. B. D. Butler and T. R. Welberry, *J. Appl. Crystallogr.* **25**, 391 (1992).